



HAL
open science

HER activity of nickel molybdenum sulfide electrocatalyst as function of the ionomer in the ink formulation

Carlos V.M. Inocêncio, Julie Rousseau, Nadia Guignard, Christine Canaff, Sophie Morisset, Teko Napporn, Cláudia Morais, K. Boniface Kokoh

► To cite this version:

Carlos V.M. Inocêncio, Julie Rousseau, Nadia Guignard, Christine Canaff, Sophie Morisset, et al.. HER activity of nickel molybdenum sulfide electrocatalyst as function of the ionomer in the ink formulation. *International Journal of Hydrogen Energy*, 2023, 48 (68), pp.26446-26460. 10.1016/j.ijhydene.2022.10.138 . hal-04285785

HAL Id: hal-04285785

<https://hal.science/hal-04285785>

Submitted on 14 Nov 2023

HAL is a multi-disciplinary open access archive for the deposit and dissemination of scientific research documents, whether they are published or not. The documents may come from teaching and research institutions in France or abroad, or from public or private research centers.

L'archive ouverte pluridisciplinaire **HAL**, est destinée au dépôt et à la diffusion de documents scientifiques de niveau recherche, publiés ou non, émanant des établissements d'enseignement et de recherche français ou étrangers, des laboratoires publics ou privés.

HER Activity of nickel molybdenum sulfide electrocatalyst as function of the ionomer in the ink formulation

Carlos V. M. Inocêncio¹, Julie Rousseau¹, Nadia Guignard¹, Christine Canaff¹, Sophie Morisset¹, Teko W. Napporn¹, Cláudia Morais^{1*}, K. Boniface Kokoh^{1*}

¹ Université de Poitiers, IC2MP, UMR-CNRS 7285, 4, rue Michel Brunet, B27, TSA 51106, 86073 Poitiers cedex 09, France.

*Corresponding authors: claudia.gomes.de.morais@univ-poitiers.fr; boniface.kokoh@univ-poitiers.fr

Highlights:

- Evidenced synergistic effect between Ni and Mo species for HER in alkaline medium
- HER performance of Ni_{0.5}Mo_{0.5}S_x can be boosted with a conduction additive
- HER performance of Ni_{0.5}Mo_{0.5}S_x strongly depends on its ink formulation.

Abstract

Transition metal sulfides (NiS_x , MoS_x and $\text{Ni}_{0.5}\text{Mo}_{0.5}\text{S}_x$) are synthesized and have their HER performance evaluated in three-electrode cell setup by applying LSV analyzes in 1 M KOH. XRD, Raman, TEM and XPS characterizations are applied aiming to correlate physicochemical properties/electrocatalytic activity. It is evidenced a synergistic effect in which nickel oxide, present in the surface of $\text{Ni}_{0.5}\text{Mo}_{0.5}\text{S}_x$, accelerates the water dissociation, while molybdenum sulfide catalyzes the reduction of adsorbed hydrogen species. When physically mixed with Carbon Vulcan, $\text{Ni}_{0.5}\text{Mo}_{0.5}\text{S}_x$ only needs 60 mV higher overpotential to achieve -200 mA cm^{-2} than 40 % Pt/C. Furthermore, $\text{Ni}_{0.5}\text{Mo}_{0.5}\text{S}_x$ activity is assessed in interaction with different ionomers (Nafion® or Sustainion® XB-7). It is shown by an exploratory study that, when Nafion® is replaced by XB-7, the amount of ionomer and water to isopropanol volume ratio must be diminished in the ink formulation to, at least, maintain a comparable activity of the electrode material.

Keywords: Transition metal electrode material; Nickel Molybdenum sulfides; water electrolysis, Hydrogen evolution reaction; ionomer effect

1. Introduction

The Sixth Assessment Report provided by IPCC in 2021 makes it clear that changes in energy sector are mandatory to envisage the control of climate change; hydrogen is pointed-out as an important energy carrier in this transition [1, 2]. However, most of industrial hydrogen production still comes from processes using fossil feedstocks, such as the steam reforming of hydrocarbons and coal gasification [3, 4]. Due to their carbon fingerprints, those processes must be replaced by decarbonized ones.

The solid polymer electrolyte water electrolysis (SPEWE) is an interesting alternative process, since if it is coupled to clean energy sources, it results in zero carbon emission. In this process, energy is supplied to the electrolyzer device, which splits water in hydrogen (H_2) and oxygen (O_2) released at the cathode and the anode compartments, respectively. These reactions are known as hydrogen evolution reaction (HER) and oxygen evolution reaction (OER), and both need the use of electrocatalysts to accelerate them, resulting in the increase of process efficiency. Noble-metal-based materials are the benchmarking catalysts for those reactions, but their high-cost and, mainly, scarcity make their use prohibitive in large-scale applications [5]. Hence, it is very important to work on the design of alternative earth-abundant catalysts that must be active, selective, and stable for the reaction.

While many catalysts produced from earth-abundant elements are not stable in acidic environment, many researchers have been devoting their attention to the development of water electrolysis in alkaline media [6-9]. However, the hydrogen evolution in high pH's has some drawbacks as the additional energy-consuming step called water dissociation, besides the interaction of generated hydroxyl groups with active sites that can play a negative role in the reaction [7, 8, 10]. Thus, a good HER electrocatalyst in alkaline media must not only show a good performance for the reduction of adsorbed hydrogen species, but also present good water dissociation skills. Previously studies reported the ability of MoS_2 to reduce protons towards molecular hydrogen [11, 12], but it lacks activity in alkaline media due to its low water dissociation performance.

In SPEWE systems, the reaction takes place in the membrane electrode assembly (MEA), which is, because of this, known as the "heart of the process". Therefore, aiming to reduce

the cost of green hydrogen production and boost the desired energetic transition, many studies are devoted to the construction of MEA increasingly efficient and at lower cost. To do so, it is important to pay attention at each part of this component. The MEA is consisted of an electrolyte membrane sandwiched by two catalyst layers, one layer responsible to perform the HER, while the other is responsible for the OER. The catalyst layers must contain the catalyst particles in good contact with ionomer because the latter one, besides to play a role as a binder, is responsible for ionic conductivity [13, 14].

Many articles show the evaluation and comparison of different membranes [15-17] and catalysts [4, 5, 9, 18] performances as main topic, however, lower attention has been addressed to the ionomer or even the interaction between the ionomer and the catalyst [14], although there are manuscripts that report its impact on catalysts activity [19-21]. Nafion® is the unanimous ionomer for applications in acidic media and, although it has its efficiency decreased in alkaline conditions [4], it is still widely used in analysis at high pH's [10, 22, 23]. Sustainion® XB-7 ionomer, called hereafter "XB-7", was developed to be used at alkaline conditions and its good behavior on water electrolysis has already been reported elsewhere [24].

Therefore, a bimetallic nickel molybdenum sulfide was synthesized herein and tested towards the HER to profit from reduction capability of molybdenum sulfide, and Ni^{2+} water dissociation skills due to its unpaired electrons in e_g orbitals [7]. Besides that, both Nafion® and XB-7 ionomers were applied in this study to investigate the influence of their use in $\text{Ni}_{0.5}\text{Mo}_{0.5}\text{S}_x$ HER performance. To the best of our knowledge, this is the first time that the electrochemical performance of a transition metal sulfide electrocatalyst in association with Sustainion® XB-7 ionomer is reported; not only considering HER, but any reaction. It was revealed that, when it replaces Nafion®, the ink must be produced with lower quantity of ionomer and the solvent must be mostly isopropanol; the complete removal of water also decreases HER activity.

2. Experimental

2.1. Catalyst preparation

Transition metal sulfide (TMS) catalysts were prepared according to the hydrothermal method reported by Li *et al.* [25] with modifications. Initially, an aqueous solution of the metallic precursor was prepared and let stirring. The nickel and molybdenum precursors employed herein were nickel chloride hexahydrate ($\text{NiCl}_2 \cdot 6 \text{H}_2\text{O}$, Sigma-Aldrich) and ammonium heptamolybdate tetrahydrate ($(\text{NH}_4)_6\text{Mo}_7\text{O}_{24} \cdot 4 \text{H}_2\text{O}$, Alfa Aesar), respectively. Simultaneously, sodium diethyldithiocarbamate trihydrate ($\text{C}_5\text{H}_{10}\text{NNaS}_2 \cdot 3 \text{H}_2\text{O}$, Alfa Aesar) was added to 20 mL of ultrapure water (Milli-Q, 18.2 M Ω cm at 20 °C) and the solution was stirred until the complete dissolution of the sulfur precursor. In the sequence, the sulfur precursor solution was slowly dripped (~1 droplet per second) into the metallic one, which was under vigorous stirring. During this dripping, solids started emerging in the metallic solution. For NiS_x synthesis, it was evidenced the appearance of green solids, while for MoS_x yellow solids were seen initially, but it started becoming orange as more droplets were added. The final mixture was then transferred to a Teflon-lined stainless-steel autoclave which was posteriorly heated at 240 °C during 24 h. Afterwards, the autoclave was let cooling down naturally before opening until a temperature close to ambient one was achieved. The material was collected after various centrifugation (six times applying 9000 rpm during 20 min) and washing steps. For the first centrifugation was done with the mixture of the hydrothermal reaction, while the two subsequent steps were performed after water washing; three other steps were required after absolute ethanol (VWR Chemicals) washing. The resulting solids were then dried at 50 °C in vacuum (50-150 mbar) overnight. Finally, they were collected and stocked to be applied in the characterizations thereafter. In the case of bimetallic sulfide, synthesized by using equimolar quantities of nickel and molybdenum (for this reason, called " $\text{Ni}_{0.5}\text{Mo}_{0.5}\text{S}_x$ " herein), the metallic solution was prepared by the direct addition of 20 mL of nickel chloride solution to 20 mL of ammonium heptamolybdate (AHM) solution, followed by vigorous stirring. Once the solution containing the sulfur precursor was dripped into the metallic solution containing both metals, green solids started appearing as well as in NiS_x synthesis. The precursor amounts and volumes applied in the synthesis of each catalyst are evidenced in Table 1.

2.2. Physico-chemical characterizations

X-ray diffraction (XRD) analyses were performed with the use of a diffractometer EMPYREAN from MALVERN PANalytical equipped with Cu K radiation source (45 kV

and 40 mA) and the linear detector PIXcel1D which works with energy discrimination; it allows not only eliminate the fluorescence effect but also delete the K-beta contribution without the use of a nickel filter. The device was operated with divergence slit and primary anti-scatter slit sizes of $1/16^\circ$ and $1/8^\circ$, respectively, and the detector was used at its maximum aperture (i.e., 3.35°). Additionally, it was applied a step size of 0.078° and time per step of 600 seconds.

Raman spectroscopy measurements were carried out at room temperature using a HORIBA JOBIN YVON Labram HR800UV Raman confocal microscope, specifically an Olympus BXM confocal microscope which enabled the operation in backscattering mode, equipped with a CCD detector cooled by the Peltier effect. For all measurements, it was applied the excitation wavelength of 532 nm, supplied by a diode-pumped solid state (DPSS) green laser, and the laser power delivered to the samples was 0.2 mW, aided by an optical density filter. In addition, 600 grooves mm^{-1} grating and the confocal pinhole diameter of 200 μm were used, resulting in a spectral resolution of 1.5 cm^{-1} . Finally, the spectrometer was calibrated with a silicon standard and the LabSpec v.5 software was used for the acquisition and treatment of data.

Transmission electron microscopy (TEM) analyses were performed in a JEOL JEM-2100 device, operated in bright field mode at 200 kV with a LaB_6 source, coupled with an energy-dispersive X-ray spectrometer containing a JEOL JED-2200 detector ($30 \text{ mm}^2 \text{ SiLi}$), enabling then the application of energy-dispersive X-ray spectroscopy (EDS) analysis. To prepare the sample for analysis, the catalyst powder was dispersed in ethanol aided by an ultrasound equipment. Subsequently, few drops of the dispersion were immediately drop-casted on a carbon-coated, holey carbon, copper TEM grid (300 mesh) and dried under vacuum. High-resolution TEM (HRTEM) images, with a resolution of 0.19 \AA , were also acquired; it allowed the calculation of interplanar distances.

X-ray photoelectron spectroscopy (XPS) analyses were carried out with a Kratos Axis Ultra DLD spectrometer using a monochromatic Al $K\alpha$ source (1486.6 eV) operating at 180 W (12 mA, 15 kV). The device was operated at $9 \times 10^{-8} \text{ Pa}$ and the charge neutralizer system was applied to all samples containing an isolating feature. High-resolution spectra were

recorded using an analysis area of 300 μm \times 700 μm , step size of 0.1 eV and 40 eV pass energy, which corresponds to Ag 3d_{5/2} full width at half maximum (FWHM) of 0.55 eV. The binding energy was calibrated using C 1s binding energy fixed at 284.8 eV as an internal reference. Peak fitting was achieved with Casa XPS software (version 2.3.24) applying Gaussian-Lorentzian profiles (Lorentzian 30%).

2.3. Electrochemical characterizations

All electrochemical measurements were performed at room temperature in a three-electrode configuration using a potentiostat device (Autolab, PGSTAT 302N). Glassy carbon slab and Hg/HgO (RE-61AP Reference electrode, ALS Co., Ltd) filled with 1 M KOH (Sigma-Aldrich) solution, were applied as counter- and reference electrodes, respectively, for all measurements. The working electrode was composed of a commercial rotating disk electrode (RDE) system (Metrohm Autolab) containing 5 mm diameter glassy carbon as substrate, onto the evaluated electrocatalysts were deposited.

The materials were attached to the electrode by preparing a catalytic ink, which was deposited onto the glassy carbon substrate and let drying for some minutes, while the electrode was stirred at 700 rpm. For the inks prepared by implementing Nafion® as ionomer, the composition consisted of 475 μL of ultrapure water, 475 μL of isopropanol (VWR Chemicals), 50 μL of Nafion® perfluorinated resin suspension (5 wt. % in lower aliphatic alcohols and water, containing 15-20 % water, Sigma-Aldrich) and 14 mg of the catalyst (or physical mixtures) analyzed, except for the commercial 40 % Pt/C (Sigma-Aldrich); in this case, 8 mg was added. For the inks prepared with XB-7® as ionomer, a variation of ink's composition was tested, the added catalyst amount was the same of the aforementioned Nafion® application though. Despite that, Equation 1, in which $V_{\text{H}_2\text{O}}$, V_{ISO} and V_{IONO} correspond, respectively, to the volumes (in μL) of water, isopropanol and ionomer suspension, was respected in all ink preparations. More importantly, it was introduced the variable R_{solv} , evidenced in Equation 2, which brings the information about water/isopropanol volume ratio. As methodology adopted to the catalytic ink formulation, initially, only water, isopropanol and ionomer suspension were added to a sample vial, which was ultrasonicated in a bath for 15 min. Subsequently, the solid material was added to the produced suspension, which was further put in ultrasound bath once more until the

homogenization of the ink was achieved (approximately, 30 min). To perform the electrochemical analyses, 7 μL of ink was deposited onto the glassy carbon substrate, therefore, the theoretical mass loading of 40 % Pt/C used in the present study was 0.28 mg cm^{-2} , while 0.50 mg cm^{-2} was applied for all other materials. It is noteworthy that these values consider the geometrical surface area of the electrode.

$$V_{H_2O} + V_{ISO} + V_{IONO} = 1000 \quad (\text{Equation 1})$$

$$R_{solv} = \frac{V_{H_2O}}{V_{ISO}} \quad (\text{Equation 2})$$

Although all measurements were performed with Hg/HgO reference electrode, the potential values reported in this document are referenced to reversible hydrogen electrode (RHE). To do so, a methodology to calibrate the Hg/HgO electrode was performed, and it is better elucidated in the supplementary information; the cyclic voltammetry used in the calibration is presented in Figure S1. As result, it was verified that 0 V vs RHE corresponded to $-0.940 \text{ V vs Hg/HgO}$, therefore, this value was used for potential conversions. Linear sweep voltammetry (LSV) analyses were performed in 1 M KOH by scanning the potential between 0.14 V and -0.56 V vs RHE at 10 mV s^{-1} , besides applying a rotation speed of 1600 rpm in the working electrode. Before any LSV measurement, electrochemical impedance spectroscopy (EIS) was performed at open-circuit potential (OCP) to obtain the solution resistance (R_s) value, which was used when ohmic drop compensation was applied. The Tafel plots were constructed with the iR-corrected data obtained from LSV analyses, but only selecting the interval in which a linear behavior relationship between overpotential (η) and the logarithm of absolute value of current density ($\log |j|$) was verified, besides to be the data associated with the beginning of the hydrogen evolution reaction (HER). The resulting curve could be fitted with Tafel equation: $\eta = a + b \log |j|$. The variable “b” corresponds to the Tafel slope, and the exchange current density (j_0) is the value of “j” when η is assumed to be zero.

3. Results and discussion

The structures of the materials were investigated by applying the XRD technique and the results are shown in Figure 1(a). For NiS_x catalyst, well-defined sharp peaks were observed;

it indicates a good crystallinity of the material. The peaks at 2θ equal 16.3° , 26.6° , 38.0° , 50.0° , 54.7° and 64.4° are related to the Ni_3S_4 phase (PDF: 43-1469), while the peaks at 27.2° , 35.3° , 38.8° , 45.1° , 53.4° , 56.0° , 58.5° and 60.9° are associated with the NiS_2 phase (ICSD: 646347). Although the most intense peak of NiS_x has its maximum at 31.5° , such peak starts to be formed at 31.0° and only finishes at 31.8° . A zoom of this peak region is presented in Figure S2 and the appearance of a contribution from two distinct peaks may be noticed, although they are superimposed. In fact, the two peaks can be associated with the most intense diffraction lines of Ni_3S_4 and NiS_2 patterns at 31.3° and 31.5° , respectively. Therefore, besides the NiS_2 phase (in agreement with synthesis stoichiometry), Ni_3S_4 , a phase poorer in sulfur, has also been detected by XRD. Both molybdenum-based sulfides presented herein showed profiles that resemble to defect-rich 2H- MoS_2 with slightly expanded (002) plane, $d(002)$ about 6.36 \AA , and containing turbostratic disorder [26-28]. Indeed, the XRD profiles of MoS_x and $\text{Ni}_{0.5}\text{Mo}_{0.5}\text{S}_x$ don't match perfectly well with 2H- MoS_2 pattern (ICSD: 601647) due to aforementioned features. The expansion of interlayer distance of (002) planes results in a shift of (002) diffraction peak and the existence of turbostratic disorder leads to the absence of (103) and (105) diffraction, replaced by large bands in those regions [29]. The XRD profile of a commercial MoS_2 well crystallized and containing none of previously mentioned characteristics is shown in Figure S3. Furthermore, additional sharp peaks, which may be associated with monoclinic nickel (II) sulfate hexahydrate (PDF: 33-955), are verified for $\text{Ni}_{0.5}\text{Mo}_{0.5}\text{S}_x$ material.

Ulbrich *et al.* [30] provided an interesting study on the phase evolution of synthesized nickel sulfide species by applying XRD technique. It was shown that, even in ambient temperature, high humidity ambient accelerated the transformation of nickel sulfide toward nickel sulfate. Therefore, it is likely that the sulfide to sulfate transformation in $\text{Ni}_{0.5}\text{Mo}_{0.5}\text{S}_x$ was boosted by the high temperature and pressure conditions applied in the hydrothermal synthesis reported herein. Nonetheless, the nickel sulfate phase was not identified in the X-ray diffractogram of NiS_x . Another point highlighted by Ulbrich *et al.* [30] is that the smaller are nickel sulfide species, the faster are their bulk oxidation. As indicated by TEM results (Figure 2), Ni-containing species are much bigger in NiS_x than in $\text{Ni}_{0.5}\text{Mo}_{0.5}\text{S}_x$. Hence, in NiS_x , sulfate formation is limited to its surface as evidenced by XPS (Figure 5e). For MoS_x ,

no sulfate is produced at all due to the high stability of MoS₂ sulfur species against oxidation [31].

The structures of the materials were also investigated by Raman spectroscopy and the results are presented in Figure 1(b). The bands at 222, 285, 339 and 379 cm⁻¹ are attributed to Ni₃S₄ [32], while those at 270, 476, 486 and 971 cm⁻¹ are assigned to NiS₂ [33, 34]. The Raman analyses were applied to different spots of NiS_x to evaluate the homogeneity of the catalyst. Figure S4(a), which evidences these spectra, shows that different proportions of aforementioned phases are identified according to the zone of the material where the analysis is applied, therefore, there is a lack of homogeneity for NiS_x. Raman spectrum of MoS_x (Figure 1(b)) evidenced remaining molybdate synthesis residue due to the presence of the band at 175 cm⁻¹ and the three other bands which appear in the 750-950 cm⁻¹ range [35-37]. It is important to highlight that such residue is not present throughout the material. As one may see in Figure S4(b), there are spots of the material in which those bands are not observed in the corresponding Raman spectra. In addition, the well-known E_{12g} and A_{1g} phonon modes of MoS₂ are present at 377 and 407 cm⁻¹, respectively [38]. These bands are also present for Ni_{0.5}Mo_{0.5}S_x, although in this case the A_{1g} mode shifts towards 403 cm⁻¹. Raman spectrum of Ni_{0.5}Mo_{0.5}S_x also exhibited a band at 298 cm⁻¹, which is assigned to E_{1g} mode of MoS₂ [39, 40], and bands in the range of 120-240 cm⁻¹ containing a profile which appears for molybdenum sulfide materials containing high density of defects [41]. Therefore, both XRD and Raman analyses show features related to defect-rich MoS₂ for the bimetallic sulfide. Finally, it can also be verified a band at 949 cm⁻¹ associated with the NiMoS₄ phase, which cannot be detected by XRD due to its amorphous character [42]. It is noteworthy that the Raman analysis was also performed in different spots of Ni_{0.5}Mo_{0.5}S_x, however, no change in the spectra were detected for this compound. Thus, the association of Ni and Mo leads to a catalyst more homogeneous in micrometric scale.

The materials were also characterized by transmission electron microscopy (TEM) to investigate their morphologies; the resulting micrographies are presented in Figure 2. NiS_x presented two distinct morphologies, three- (Figure 2(a)) and two-dimensional (Figure 2(b)) crystals. Negligible amount of oxygen was detected in this material by the application of energy-dispersive X-ray spectroscopy (EDS) analysis. The MoS_x material presented sheet

morphology, typical of MoS₂ (Figure 2(c)). Besides that, the sheets can be divided into two groups, one containing very stacked large MoS₂ sheets (Figure 2(d)) and another corresponding to well-dispersed few-layer MoS₂ nanosheets (Figure 2(e)), which is the most interesting morphology for HER application. Ni_{0.5}Mo_{0.5}S_x exhibited a similar trend of MoS_x. In Figure 2(f), it can be seen the sheets containing different agglomeration and stacking degrees. The larger sheets containing elevated stacking degree are evidenced in Figure 2(g), while the few-layer nanosheets are shown in Figure 2(h). Additionally, Ni_{0.5}Mo_{0.5}S_x contains crystallized larger particles (Figure 2(i)) which are rich in nickel and sulfur according to EDS analysis. Such particles were attributed to the existence of nickel sulfate species detected by XRD.

In addition, HRTEM images of molybdenum-based sulfides were acquired and interplanar spacings were measured. Figure 3 shows distances of 0.63 and 0.62 nm in MoS_x and Ni_{0.5}Mo_{0.5}S_x nanosheets, respectively. These distances are associated with (002) plane distance of 2H-MoS₂ phase, also identified by XRD. Yet, these distances are close, bearing in mind the equipment resolution, to the calculated by XRD taking into consideration the diffraction peak of (002) plane. An interplanar spacing of 0.26 nm is also verified for the Ni_{0.5}Mo_{0.5}S_x HRTEM micrograph (Figure 3(b)), which is related to the (100) plane of 2H-MoS₂. Therefore, HRTEM micrographs provide more evidence about the presence of 2H-MoS₂ in molybdenum-containing catalysts. HRTEM image of NiS_x was also obtained and d-spacings were measured as shown in Figure S6. However, due to the similarity between distances of NiS₂ and Ni₃S₄ planes [43], it is not possible to distinguish which of the phases are present in the image.

In order to investigate the dispersion of elements in Ni_{0.5}Mo_{0.5}S_x, an elemental mapping was generated from applying EDS technique in transmission electron microscope; resultant images are shown in Figure 4. As one may see, all elements, including oxygen (as expected due to the presence of sulfate), are well dispersed in this bimetallic sulfide. Such analysis was also extended to NiS_x and MoS_x materials and the results are presented in Figures S7 and S8, respectively. Interestingly, nickel and sulfur also showed good dispersion for NiS_x, however, less oxygen is detected in this material when compared to Ni_{0.5}Mo_{0.5}S_x; this trend matches with results obtained by XRD. On the contrary, good dispersion of molybdenum,

sulfur and oxygen was registered for MoS_x . This result is not surprising since the existence of molybdate residues in MoS_x was verified by Raman spectroscopy.

The chemical nature at the surface of the catalysts was studied by XPS and the resulting spectra are depicted in Figure 5. The Ni 2p spectrum of NiS_x (Figure 5(a)) exhibited three peaks that could be deconvoluted by the contribution of three doublets. The major contribution came from the NiS_2 species [44] which were also verified by XRD and Raman results. The contact with air led to an oxidation of the NiS_x surface resulting in the formation of nickel oxide [45] and, in less quantity, nickel sulfate species. The existence of nickel sulfate in the surface was also clearly revealed by the analysis of S 2p spectrum of NiS_x (Figure 5(e)). Besides that, contributions related to S_2^{2-} and S^{2-} species were also detected [46]. To unveil the contributions of nickel sulfate in Ni 2p and S 2p spectra, a commercial nickel sulfate heptahydrate was analyzed by XPS measurements and their spectra are presented in Figure S9.

As seen in Figure 5(c), molybdenum was present in three oxidation states at the surface of MoS_x . The highest contribution came from Mo^{4+} , typical of MoS_2 species; Mo^{5+} and Mo^{6+} were also present in similar quantities [45]. MoS_2 may also suffer oxidation derived from the air-contact which leads to the formation of MoO_3 , in which molybdenum is present with an oxidation state equal +6. It is noteworthy that Raman analysis also identified remaining Mo-O linkages which can also be related to the state +6. It has already been reported that the existence of Mo^{5+} can be attributed to existence of molybdenum oxysulfide. It is, in fact, an intermediate specie between molybdenum sulfide and molybdenum oxide and, therefore, its presence can be associated with molybdate that was not completely sulfurized [47] or MoS_2 which has been only partially oxidized. The S 2p spectrum of MoS_x (Figure 5(f)) exhibited negligible contribution from sulfates and the existence of S_2^{2-} [47] in low quantities. This latter specie is generally associated with molybdenum sulfides containing low degree of crystallinity. In fact, for this spectrum, the major contribution came from S^{2-} as expected for MoS_2 [47].

Contrary to NiS_x , according to Ni 2p spectrum of $\text{Ni}_{0.5}\text{Mo}_{0.5}\text{S}_x$ (Figure 5(b)), most of nickel in this compound was present in an oxidized form; mostly as oxide [45], but also as sulfate.

Despite that, although in lower quantity, a tertiary sulfide containing nickel, molybdenum and sulfur was also verified [45], which is likely associated with the NiMoS₄ phase also detected by Raman spectroscopy. Figure 5(d), which shows the Mo 3d spectrum of Ni_{0.5}Mo_{0.5}S_x, elucidates that, as well as for MoS_x, the curve can be fitted by the contribution of Mo⁴⁺, Mo⁵⁺ and Mo⁶⁺ species [45]. However, in the bimetallic sulfide, the contribution from the Mo⁴⁺ oxidation state, typical of MoS₂ materials, is even higher. Small contribution of Mo⁶⁺ may be associated with the existence of the previously cited NiMoS₄ phase, but the possibility of MoO₃ coexistence due to molybdenum oxidation in contact with air may not be discarded. As explained above, the Mo⁵⁺ oxidation state is related to molybdenum surrounded by oxysulfidic species [47]. Finally, the S 2p spectrum of Ni_{0.5}Mo_{0.5}S_x, presented in Figure 5(g), showed that most sulfur species were present as S²⁻ ligands, as expected for MoS₂ phase [47]. The presence of sulfate groups was also evident, in agreement with the Ni 2p spectrum (Figure 5(b)). In minority, the S₂²⁻ ligands, bridging and terminal [47], were also present, although in lower quantity than that detected for a MoS_x material.

Therefore, according to XPS results, nickel present in the bimetallic sulfide was more susceptible to oxidation than in NiS_x. Despite that, the existence of a tertiary sulfide phase (likely NiMoS₄) was verified for Ni_{0.5}Mo_{0.5}S_x. Another important point is that, although the nickel oxides and sulfates were extensively present on the surface of Ni_{0.5}Mo_{0.5}S_x, the incorporation of nickel in the synthesis led to MoS₂ phase less oxidized than the one obtained to MoS_x, which contained higher contents of Mo⁵⁺ and Mo⁶⁺.

The materials have their activities towards HER tested by LSV measurement in 1 M KOH at 10 mV s⁻¹ and 1600 rpm; the resulting curves are depicted in Figure 6(a). It became evident that the glassy carbon (GC) electrode is not active at all, and it was only used as a substrate to deposit the active materials. The monometallic sulfides, MoS_x and NiS_x, showed to be active for the reaction and requested 285 and 300 mV of overpotential to achieve -10 mA cm⁻². In addition, while the first one could not achieve -100 mA cm⁻² during the experiment, i.e., at overpotentials lower than 560 mV, the second one delivered this value at 513 mV. By the inset graph in Figure 6(a), one may see that MoS_x started the HER at slightly lower overpotential than NiS_x. However, considering the Tafel plot (Figure 6(b)) derived from the polarization curve, it may be inferred that NiS_x presents a better HER kinetics than MoS_x,

once the former exhibited a Tafel slope about 112 mV dec^{-1} and the calculated value for the latter was about 131 mV dec^{-1} . For this reason, NiS_x presented a better activity at higher current densities. The bimetallic $\text{Ni}_{0.5}\text{Mo}_{0.5}\text{S}_x$ also showed to be active towards the HER and presented an **onset** overpotential lower than both monometallic sulfides. Furthermore, the values of η_{10} and η_{100} registered on the polarization curve for $\text{Ni}_{0.5}\text{Mo}_{0.5}\text{S}_x$ were 203 mV and 500 mV, respectively. It is important to highlight that the water dissociation step is of paramount importance for HER in alkaline media. MoS_2 is well-known for being an excellent electrocatalyst for proton reduction, but it presents low performance for water dissociation [48, 49]. Additionally, XPS measurements evidenced a higher concentration of nickel oxide on the surface of $\text{Ni}_{0.5}\text{Mo}_{0.5}\text{S}_x$ when compared to NiS_x . Generally, the oxidation of sulfides is an undesired process, however, Boettcher group [50] showed that nickel oxide, which is hydroxylated in alkaline environment, is an excellent water dissociation catalyst. Therefore, in fact, the nickel oxide at the surface of $\text{Ni}_{0.5}\text{Mo}_{0.5}\text{S}_x$ is responsible for the water dissociation and, consequently, for producing the hydrogen adsorbed specie that will be further reduced to H_2 on molybdenum sulfide active sites. The lower overpotentials registered for $\text{Ni}_{0.5}\text{Mo}_{0.5}\text{S}_x$ can clearly be explained, compared to those observed on the surface of the monometallic sulfides. It can be noticed that the beginning of hydrogen evolution is overlaid with a reduction process for $\text{Ni}_{0.5}\text{Mo}_{0.5}\text{S}_x$. This reduction only appears in the first cycle of LSV analysis and is attributed to the reduction of oxidized species at the surface of the electrocatalyst. Therefore, in order to obtain the Tafel plot for $\text{Ni}_{0.5}\text{Mo}_{0.5}\text{S}_x$, the necessary data were extracted from the second scan polarization curve shown in Figure S10. Figure 6(b) displays the Tafel plots of the different investigated electrode materials; among them the Tafel slope (b) of $\text{Ni}_{0.5}\text{Mo}_{0.5}\text{S}_x$ is 78 mV dec^{-1} . This is the only material reported herein in which the second polarization curve was used for the calculations, all the others had their data extracted from the first scan. By applying only η_{10} , η_{100} and b as activity descriptors, it could be concluded that the $\text{Ni}_{0.5}\text{Mo}_{0.5}\text{S}_x$ cathode is more active than both NiS_x and MoS_x . Nonetheless, at -0.56 V vs RHE the NiS_x electrocatalyst delivered 133 mA cm^{-2} current density, while at the same potential the current density obtained on $\text{Ni}_{0.5}\text{Mo}_{0.5}\text{S}_x$ was 126 mA cm^{-2} ; this activity inversion is noticed from -0.54 V vs. RHE onwards.

Despite the synthesized sulfide materials are active for the HER, their performance is still far from the one verified for the commercial (Sigma Aldrich) 40% Pt/C, which was also

analyzed during the work as a reference electrocatalyst for HER. From the polarization curve (Figure 6(a)), the values of η_{10} , η_{100} and η_{200} were equal 46 mV, 288 mV and 481 mV for this material; in addition, it was verified a Tafel slope about 37 mV dec⁻¹ (Figure 6(b)). The aforementioned descriptors of 40% Pt/C showed values much lower than the ones obtained for the sulfides, however, it is necessary to keep in mind the influence of electrocatalysts conductivity on their activity [51]. Although some metal sulfides may present metallic properties, e.g. the 1T-MoS₂ phase [52, 53], all the transition metal sulfide (TMS) phases identified herein exhibit semiconductive nature [33, 34, 54, 55]. Such conductivity issue may be overcome by mixing physically the semiconductor catalyst with Carbon Vulcan XC72R material, which acts as a conduction additive. Thus, this physical association of materials was tested for NiS_x and Ni_{0.5}Mo_{0.5}S_x since they presented the best activities at elevated current density values. Although the onset potential of NiS_x was maintained in the physical mixture with Carbon Vulcan XC72R, its activity was reduced as evidenced in Figure 6(a). This physical mixture needed overpotentials 39 mV and 33 mV higher than only NiS_x to achieve -10 mA cm⁻² and -100 mA cm⁻², respectively. Moreover, no relevant alteration on the value of Tafel slope was noticed as result of Carbon Vulcan addition (Figure 6(b)). Concerning the Tafel slope, the same behavior was noticed for the addition of Carbon Vulcan to the ink formulation of Ni_{0.5}Mo_{0.5}S_x. From Figure 6(a), it is evident that the value of η_{10} for Ni_{0.5}Mo_{0.5}S_x is the same in the presence and absence of Carbon Vulcan and the onset overpotential also seems to be equal; nonetheless, the reduction process observed in the curve registered in the absence of Carbon Vulcan becomes an inconclusive admeasurement. Therefore, a graph was plotted with the results of the second scans with LSV technique and it is exhibited in Figure S10. This figure allows to confirm the maintenance of the same overpotential; therefore, it does not depend on the presence of Carbon Vulcan. Despite the aforementioned descriptors did not alter with the use of Carbon Vulcan, its addition effect became clear at high current densities, exactly in the operation condition that conductivity feature is even more relevant. A reduction of 98 mV in overpotential to achieve -100 mA cm⁻² was obtained with the conduction additive. Furthermore, it should be noted that this physical mixture containing Ni_{0.5}Mo_{0.5}S_x and Carbon Vulcan, with mass ratio equal 1:1, only requested an overpotential 60 mV higher than the 40% Pt/C catalyst to achieve a current density of 200 mA cm⁻². Thus, bearing in mind the cost of catalyst production, this physical mixture emerges as an interesting

electrocatalyst candidate to be applied on the cathode of anion exchange membrane water electrolyzer (AEMWE) devices. The Carbon Vulcan was also evaluated on HER, but it presented negligible activity as shown in **Figure 6(a)**. Hence, it can be concluded that even in the physical mixtures, the activity keeps coming from the sulfides and the Carbon Vulcan aids by enhancing the electroconductivity. The values of η_{10} , η_{100} , η_{200} and b for all materials are summarized in Table 2.

An interesting aspect of the use of Carbon Vulcan in the ink preparation was the fact that it worked very well for $\text{Ni}_{0.5}\text{Mo}_{0.5}\text{S}_x$, although it reduced the activity when combined with NiS_x . It is of paramount importance to consider that, once the mass loading of material was maintained constant in the analyses, the addition of Carbon Vulcan led to a reduction of the quantity of TMS in the electrode, which are the real active species for the reaction. Thus, it may be assumed that the enhancement of conductivity provoked by the Carbon Vulcan addition was not enough to compensate the lower quantity of NiS_x HER active sites. On the other hand, such conductivity enhancement on the combination with $\text{Ni}_{0.5}\text{Mo}_{0.5}\text{S}_x$ was likely more relevant than the decrease of available active sites. Despite the sulfide species highlighted in this work present semiconductive nature, it does not mean that they possess the same conductivity. We hypothesize that the Ni content may play a role in the conductivity; the more nickel, the more conductive. Such behavior has already been noticed and reported by Xu *et al.* [51] for oxides containing iron group elements. In this study, NiCoO_x and NiCoFeO_x showed much higher conductivity than Co_3O_4 and CoFeO_x . Since a conduction additive would impact the catalytic behavior more as less conductive is the material, assuming that the reaction kinetics is limited by the conductivity in the absence of the aforementioned additive, the previously hypothesis may justify the improvement of performance for $\text{Ni}_{0.5}\text{Mo}_{0.5}\text{S}_x$ and not for NiS_x . Nonetheless, the increase of activity by the association of NiS_x and Carbon Vulcan is not verified in **Figure 6(a)** because current density is obtained by geometrical surface normalization. In **Figure S11** the same results were plotted, but at this time normalizing the current by the mass of active compounds (carbon-based species were not considered). At elevated overpotentials the physical mixture ($\text{NiS}_x + \text{XC72R}$) exhibited higher absolute values of current density than NiS_x . Since the number of active sites is proportional to the mass loading of NiS_x , it is evident that the reaction became faster in the NiS_x sites for the physical mixture.

Due to the importance of a good interaction between catalyst and ionomer species, additional electrochemical experiments were done with XB-7 ionomer and these results were compared to the ones obtained by applying Nafion®. Because of the benchmark status attributed to Pt as HER catalyst, it was decided to initiate this comparison with the reference 40% Pt/C electrocatalyst. The catalytic ink was prepared with the same methodology, even same volumes, only replacing the Nafion® suspension by the XB-7 one. LSV analysis was then applied once more and a comparison of activity with each ionomer is presented in Figure 7(a). Although the onset overpotential of 40% Pt/C kept unaltered, it is clear that XB-7 led to higher current densities than Nafion®. The use of XB-7 reduced the values of η_{100} and η_{200} in 50 and 73 mV, respectively. Before the LSV analyses, cyclic voltammetry (CV) technique was applied and the results for the use of Nafion and XB-7 are presented in Figure S12(a). The charge associated with the electrochemical oxidation of monolayers of hydrogen adsorbed species (Q_H) [56] were calculated. The ratio of charges (Q_H^{XB-7}/Q_H^{Nafion}) verified was equal 1.21, therefore, the interaction between 40% Pt/C and XB-7 resulted in an increase of Pt active sites' availability of around 21% in comparison with Nafion® application; it may justify the activity enhancement.

The same methodology was applied to $Ni_{0.5}Mo_{0.5}S_x$ electrocatalyst once it was the most interesting synthesized material reported herein. Figure 7(b) exhibits the uncompensated polarization curves for the electrodes prepared from inks containing 50 μ L of ionomer and water to propanol volume ratio (R_{solv}) equal 1. Unexpectedly, the material prepared with the ink containing XB-7 performed worse than the electrode containing the Nafion® ionomer. A current density of -126 mA cm^{-2} could be achieved at -0.56 V vs. RHE , while, approximately, half of this values was obtained at the same potential for the electrode containing XB-7. Once there are a large variety of ink recipes and their effectiveness depends on the type of catalyst in use [21], it was decided to vary some parameters on the catalytic ink recipe containing XB-7 in order to investigate their effect on HER activity of $Ni_{0.5}Mo_{0.5}S_x$.

Figure 7(c) exhibits the results obtained for electrodes, in which the deposited inks were prepared with different volumes of XB-7 suspension. The graph shows that the electrode prepared with 20 and 50 μ L of XB-7 presented similar activity, however, for the intermediate

value of 30 μL , a better HER activity was achieved. The variation of activity as function of the ionomer content was also reported by Faid *et al.* [20] for Ni/C HER catalyst, although the variation of the same ionomer content, Fumatech Fumion FAA-3, had no major impact on the activity of NiO catalyst toward OER. In **that** study, the variation was attributed to the agglomeration of Ni/C on the electrode surface as verified by scanning electron microscopy (SEM).

Different recipes containing 30 μL of XB-7 and varying the R_{solv} parameter were prepared aiming to investigate the effect of this last one on $\text{Ni}_{0.5}\text{Mo}_{0.5}\text{S}_x$; results are depicted in **Figure 7(d)**. It may be seen that, when water is present in more quantity ($R_{\text{solv}} = 2$) on the ink composition, $\text{Ni}_{0.5}\text{Mo}_{0.5}\text{S}_x$ presented the lowest activity. Furthermore, when isopropanol was applied as the only solvent ($R_{\text{solv}} = 0$), the activity was lower than for the ink prepared from equal volumes of water and isopropanol ($R_{\text{solv}} = 1$). However, the catalytic ink prepared from the addition of double of isopropanol in relation to water ($R_{\text{solv}} = 0.5$) showed the best activity. Such behavior, i.e., higher activities for electrodes prepared from ink containing low water/alcohol ratio, is typical of hydrophobic catalysts [21]. This interaction among water, isopropanol, ionomer and the catalyst is very important because it will directly impact the quality of catalyst layer deposited onto the electrode substrate and, consequently, the dispersion of the catalyst, which is an important parameter in catalysis.

By looking back to **Figure 7(b)**, one may see that, at potentials lower than -0.4 V vs. RHE, the electrode prepared from the deposition of an ink containing 30 μL of XB-7 and $R_{\text{solv}} = 0.5$ achieved slightly higher current densities than the one obtained from the use aforementioned Nafion-containing ink. Despite that, from the CV measurements (varying scan rate from 20 to 60 mV s^{-1}) registered in the capacitive region of these electrodes, shown in **Figures S12(b) and S12(c)**, respectively, the capacitances were calculated. Interestingly, the electrode prepared with the Nafion ionomer showed a capacitance about 7 times higher than that with XB-7. Considering the relationship between capacitance and electrochemical surface area (ECSA), it can be concluded that the electrode containing XB-7 showed a similar activity, although it had a lower availability of active sites. Besides the effects already mentioned here, sometimes the ionomer may act by changing the chemical nature of the catalyst at the surface [19] or even may poison the catalyst by blocking its active sites [57,

58]. Further characterizations must be performed to better understand the Ni_{0.5}Mo_{0.5}S_x/XB-7 interaction.

This is an exploratory study of the influence of some parameters of ink preparation in HER activity, which is intended to continue aiming the optimization of catalytic ink for Ni_{0.5}Mo_{0.5}S_x. The aim of its exposition is to elucidate the relevance of studying catalyst/ionomer interactions to achieve superior activities. It is expected that these results can encourage the research community to investigate deeper the catalyst/ionomer interface, which can bring essential information to consolidate the AEMWE technology.

4. Conclusion

Monometallic (NiS_x and MoS_x) and bimetallic (Ni_{0.5}Mo_{0.5}S_x) sulfides were synthesized by applying a hydrothermal synthetic methodology in which sodium diethyldithiocarbamate was used as sulfur source. All of them showed to be HER active electrocatalysts, although lower overpotential descriptors were obtained for Ni_{0.5}Mo_{0.5}S_x. This behavior was attributed to the existence of nickel oxide species on the surface, according to XPS results, as well as molybdenum sulfide containing lower oxidation degree. While the first is an excellent water dissociation catalyst, MoS_x is one of the most active catalysts for the reduction of adsorbed hydrogen species to molecular hydrogen; therefore, a synergy effect emerges from their combination. Furthermore, Ni_{0.5}Mo_{0.5}S_x performance at high overpotentials was boosted by physically mixing it with Carbon Vulcan XC72R, which played a role as conduction additive. As result, this physical mixture requested an overpotential only 60 mV higher than the benchmarking 40 % Pt/C electrocatalyst to achieve 200 mA cm⁻². Therefore, Ni_{0.5}Mo_{0.5}S_x is presented herein as an interesting candidate to replace Pt-based catalysts in the cathode of anion exchange membrane water electrolyzers, due to its earth-abundance and low cost. Finally, Ni_{0.5}Mo_{0.5}S_x HER performance was studied in function of catalytic ink formulation using two different ionomers, more precisely Nafion[®] and XB-7. The exploratory study showed that, when Ni_{0.5}Mo_{0.5}S_x is applied as HER catalyst, to improve catalyst's performance by replacing Nafion by XB-7, it is necessary to reduce the amount of ionomer and water/isopropanol volume ratio; the same adjustment was not necessary for 40 % Pt/C. It reveals that the interaction between a catalyst and an ionomer is unique, and it also

depends on ink's production methodology. Therefore, this work sheds light on the importance of specific ink formulations' development according to the electrocatalyst employed, which requires a deep understanding of electrocatalyst/ionomer interface.

Figures

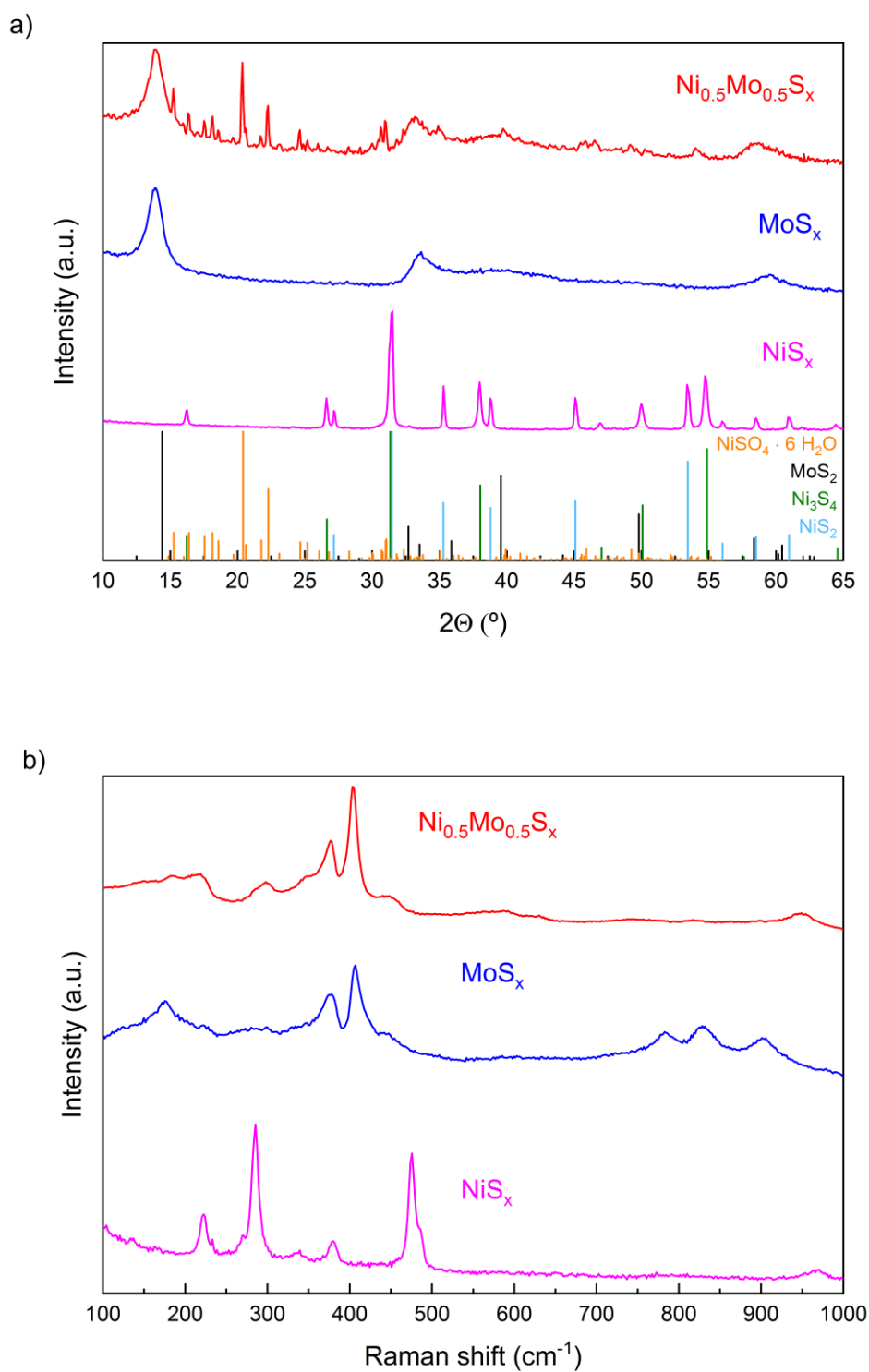


Figure 1 – (a) X-ray diffractograms and (b) Raman spectra of synthesized monometallic and bimetallic sulfides.

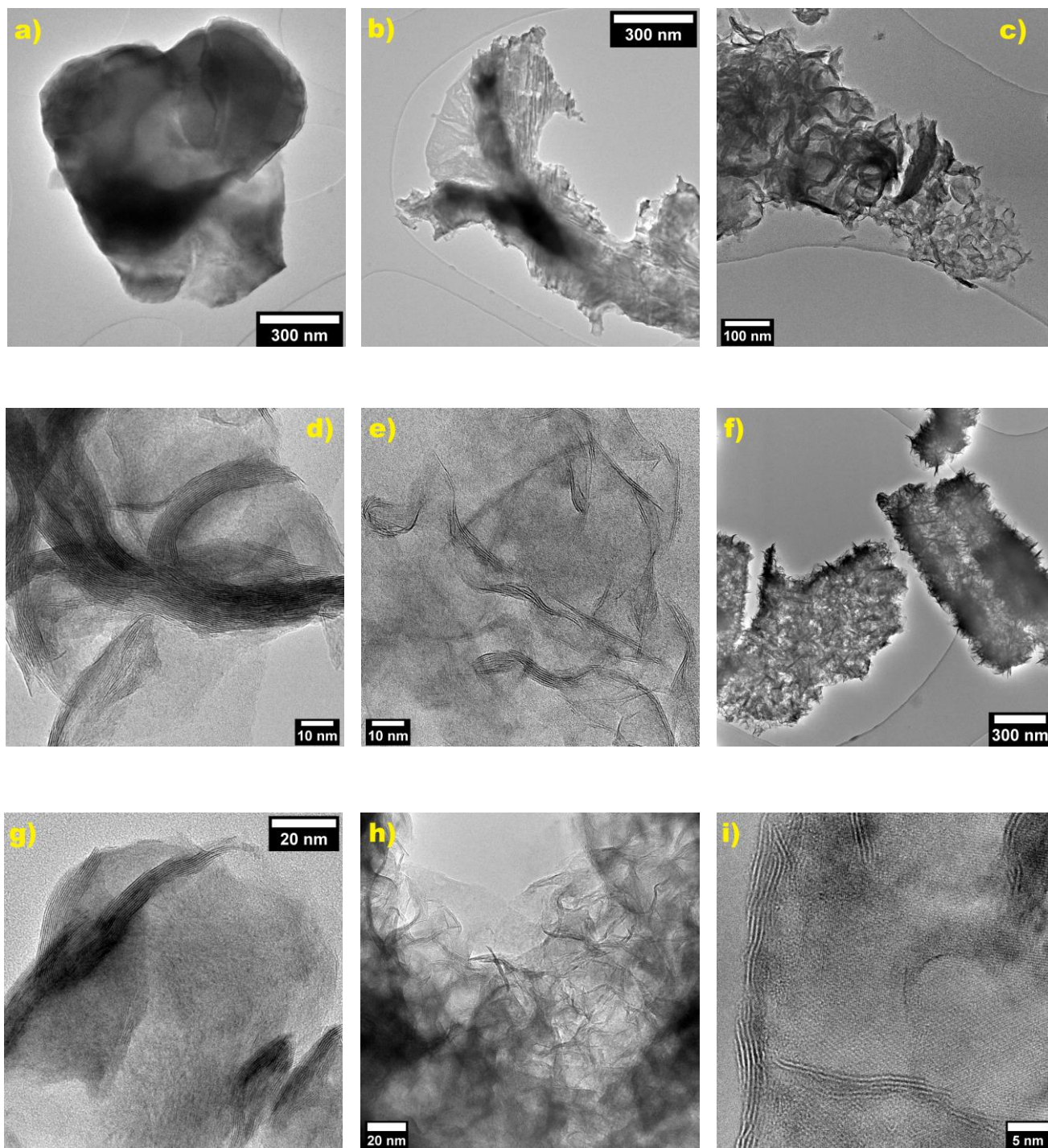


Figure 2 – TEM images of (a,b) NiS_x , (c, d,e) MoS_x and (f, g, h,i) $Ni_{0.5}Mo_{0.5}S_x$.

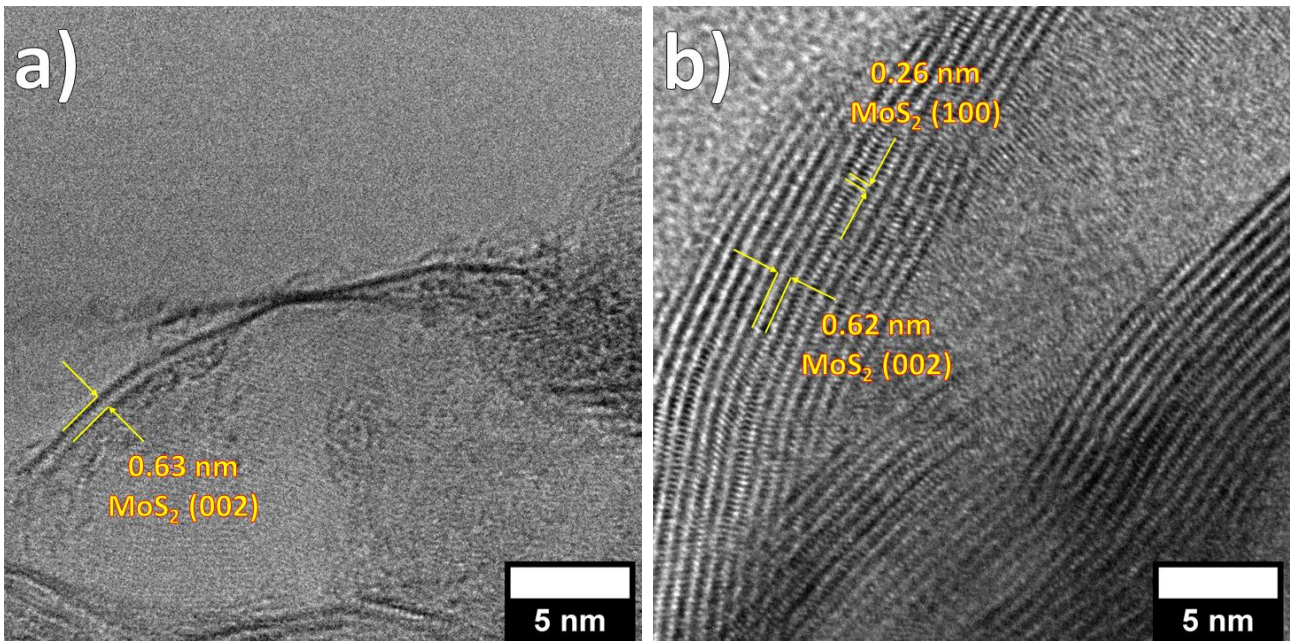


Figure 3 – HRTEM micrographs of (a) MoS_x and (b) $\text{Ni}_{0.5}\text{Mo}_{0.5}\text{S}_x$.

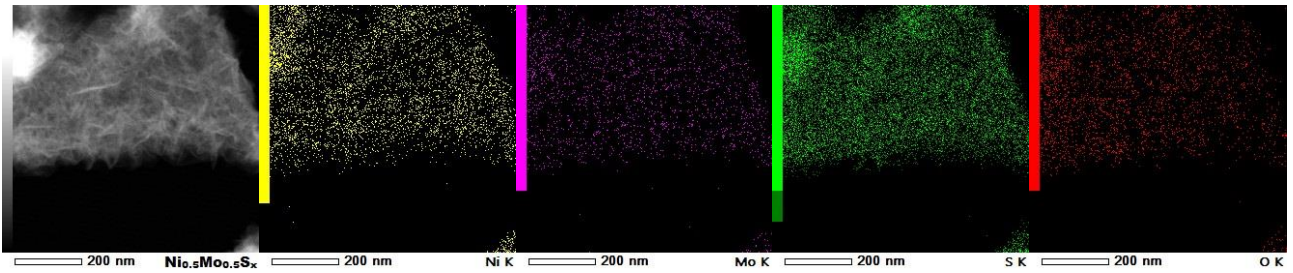
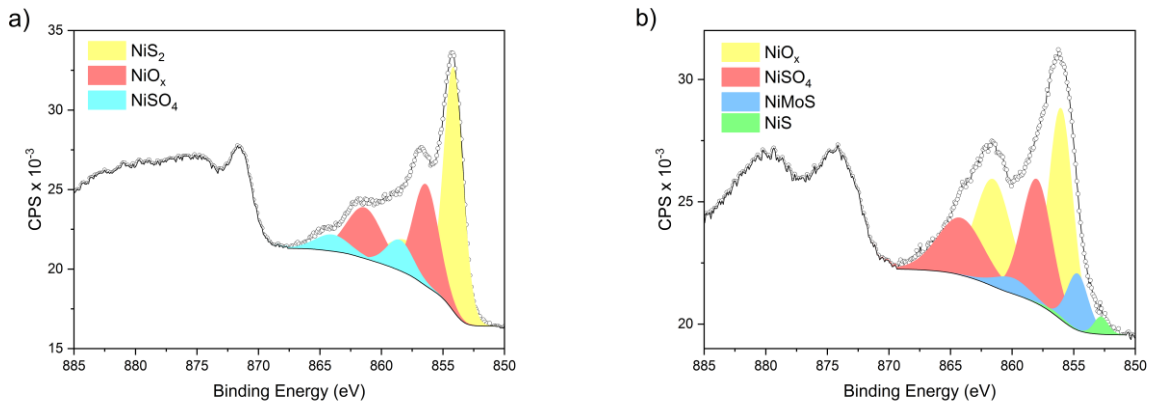


Figure 4 – Elemental mapping of $\text{Ni}_{0.5}\text{Mo}_{0.5}\text{S}_x$. Gray scale image represents the original figure, while the images in yellow, violet, green and red were generated according to the spots where nickel, molybdenum, sulfur and oxygen, respectively, were identified.



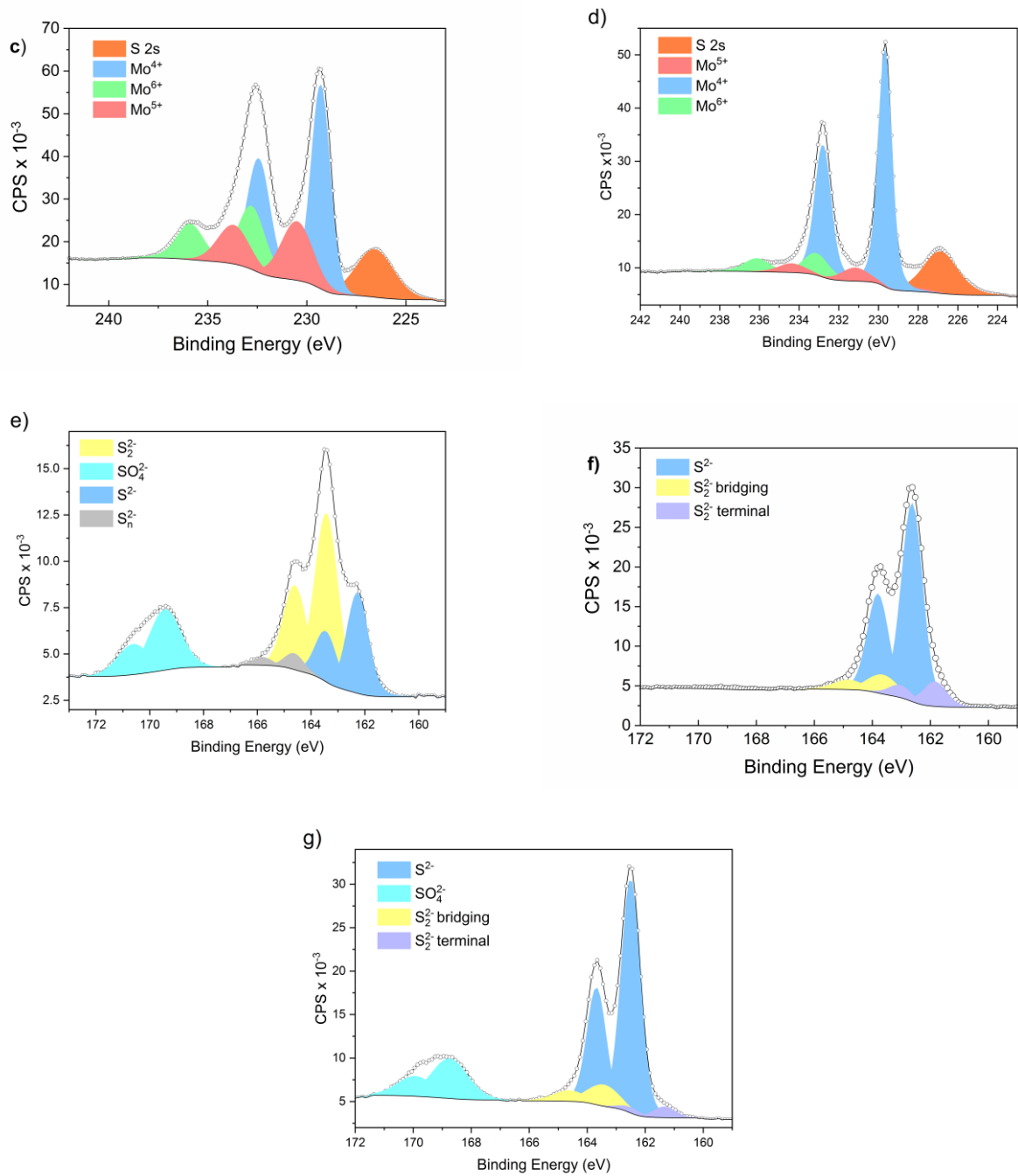


Figure 5. Ni 2p spectra of (a) NiS_x and (b) $\text{Ni}_{0.5}\text{Mo}_{0.5}\text{S}_x$, Mo 3d of (c) MoS_x and (d) $\text{Ni}_{0.5}\text{Mo}_{0.5}\text{S}_x$ and S 2p spectra of (e) NiS_x , (f) MoS_x and (g) $\text{Ni}_{0.5}\text{Mo}_{0.5}\text{S}_x$.

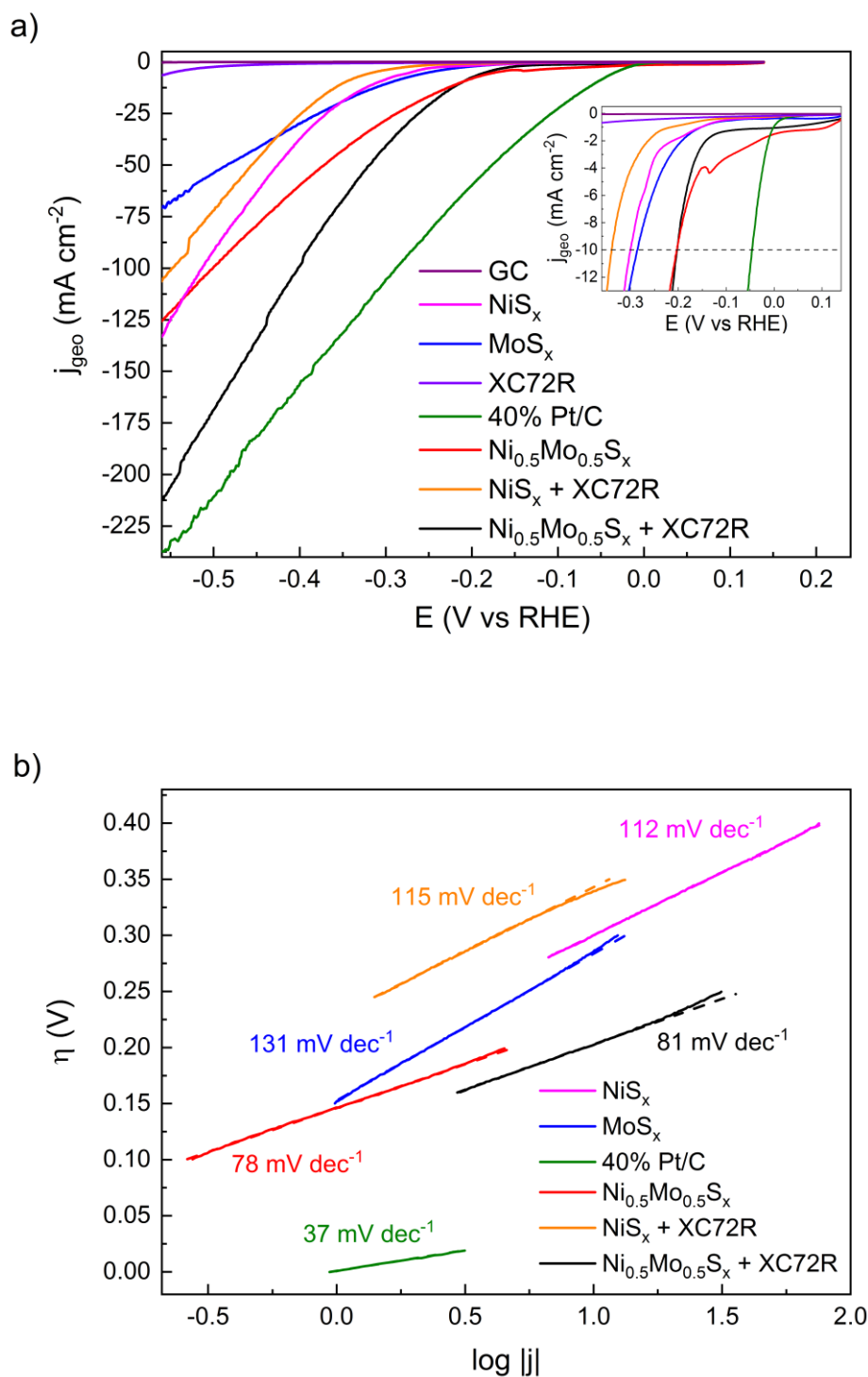
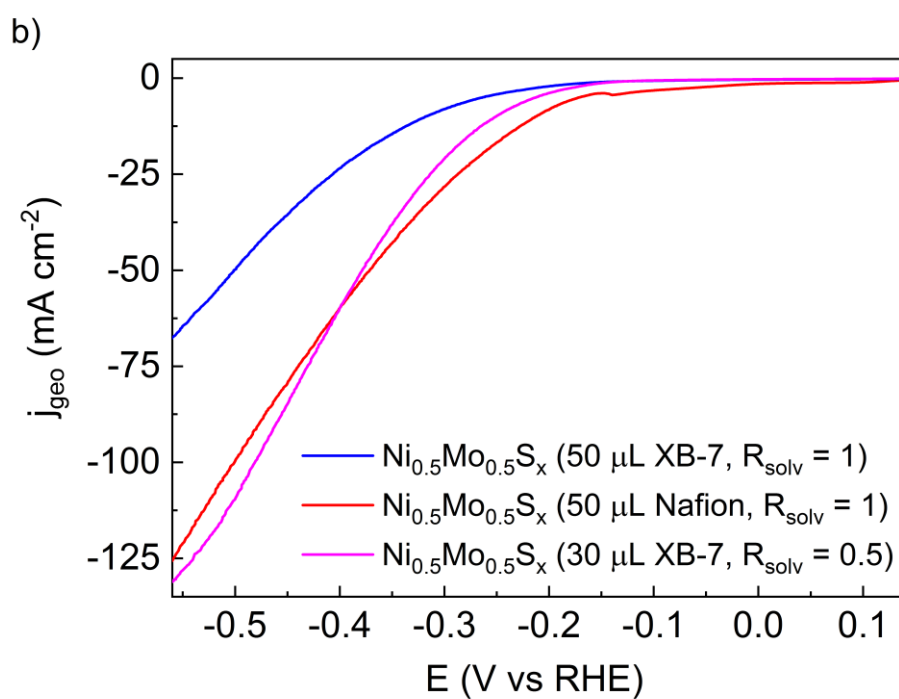
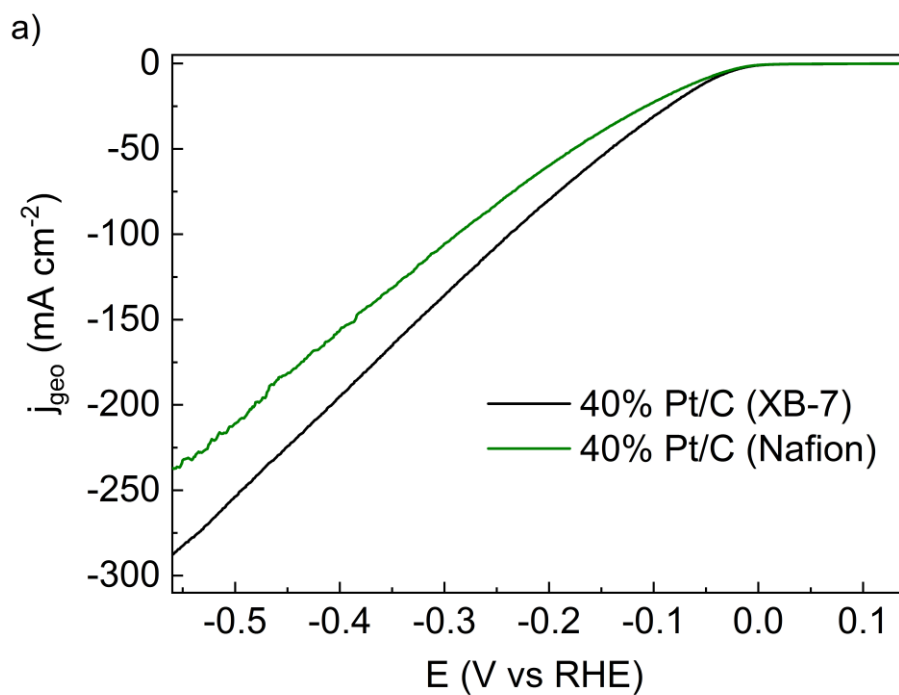


Figure 6 – (a) Uncompensated polarization curves for HER in 1 M KOH at 1600 rpm. Inset: *iR*-drop compensated curves at low current densities. (b) Tafel plot derived from the *iR*-corrected polarization curves. *The Tafel plot of $\text{Ni}_{0.5}\text{Mo}_{0.5}\text{S}_x$ was obtained from 2nd scan.



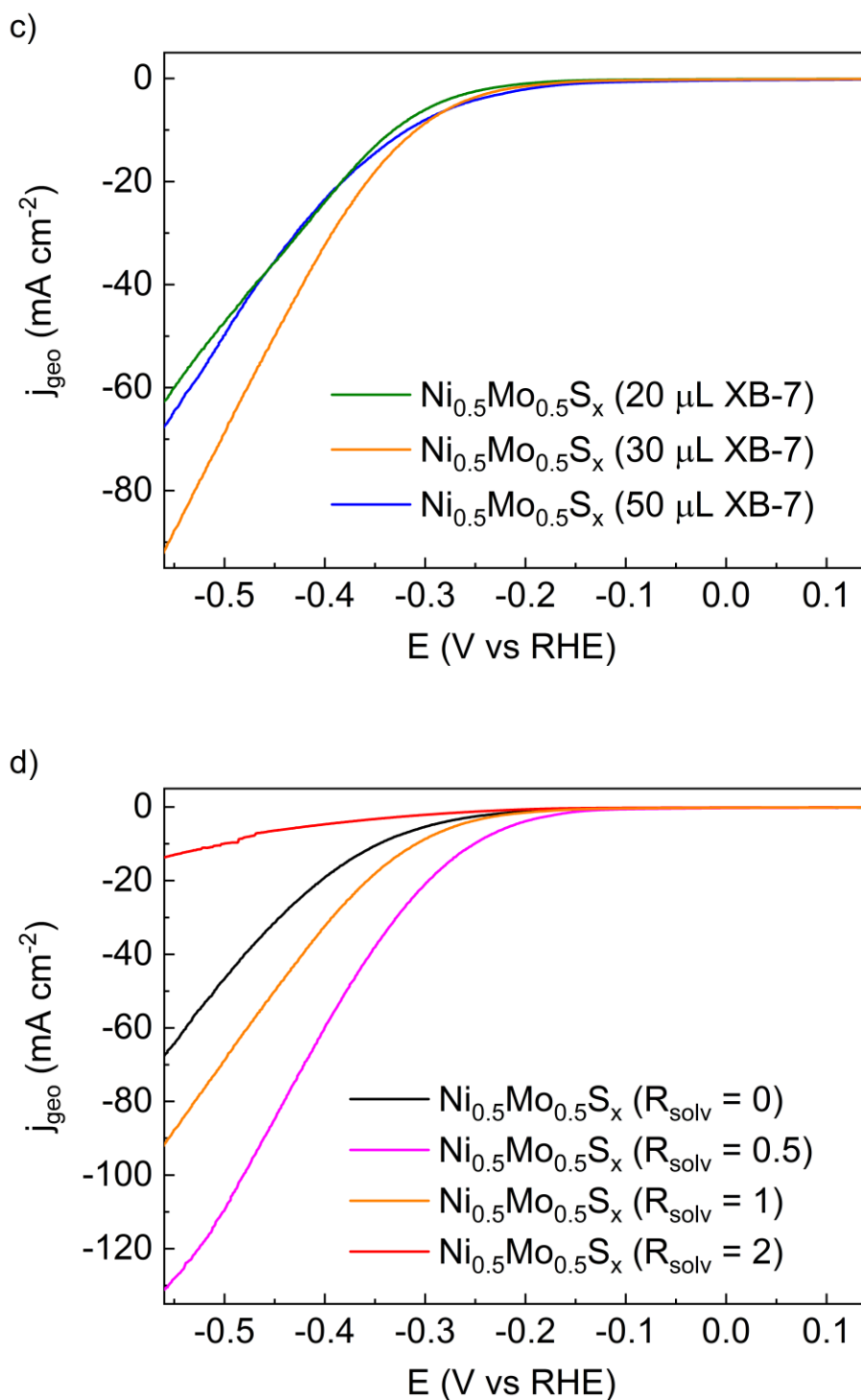


Figure 7 – Uncompensated polarization curves for HER in 1 M KOH at 1600 rpm. (a) Comparison of 40% Pt/C electrocatalysts activity according to the ionomer suspension applied; catalytic ink prepared with 50 μL of ionomer suspension and $R_{\text{solv}} = 1$. (b) Comparison of $\text{Ni}_{0.5}\text{Mo}_{0.5}\text{S}_x$ activity by the use of different ionomer suspensions. (c) The influence of XB-7 suspension volume added to the ink containing $R_{\text{solv}} = 1$ on the activity of $\text{Ni}_{0.5}\text{Mo}_{0.5}\text{S}_x$. (d) Influence of R_{solv} parameter on the activity of $\text{Ni}_{0.5}\text{Mo}_{0.5}\text{S}_x$ electrocatalysts prepared from inks produced with the addition of 30 μL of XB-7 suspension.

Tables

Table 1. Quantities of precursors and volumes applied in the synthesis of the unsupported transition metal sulfides

Catalyst	NiS _x	MoS _x	Ni _{0.5} Mo _{0.5} S _x
n_{NC} (mmol)	2.00	0	1.00
n_{AHM} (mmol)	0	0.28	0.14
n_{SDEDTC} (mmol)	2.00	2.00	2.00
V_{NC} (mL)	40	0	20
V_{AHM} (mL)	0	40	20
V_{SDEDTC} (mL)	20	20	20

*n_x = quantity of compound "X", V_x = volume of solution "X", NC = nickel chloride, AHM = ammonium heptamolybdate and SDEDTC = sodium diethyldithiocarbamate.

Table 2. Parameters values obtained from LSV analyses in HER region.

Catalyst	NiS _x	MoS _x	Ni _{0.5} Mo _{0.5} S _x	NiS _x + XC72R	Ni _{0.5} Mo _{0.5} S _x + XC72R	40% Pt/C
η₁₀ (mV)	300	285	203	339	203	46
η₁₀₀ (mV)	513	-	500	548	402	288
η₂₀₀ (mV)	-	-	-	-	541	481
b (mV dec⁻¹)	112	131	78 ^a	115	81	37

*η₁₀ and b were obtained after iR-compensation, while η₁₀₀ and η₂₀₀ are related to non-compensated results.

^aValue calculated from the second scan of LSV analysis.

References

- [1] Zhang H, Maijenburg AW, Li X, Schweizer SL, Wehrspohn RB. Bifunctional Heterostructured Transition Metal Phosphides for Efficient Electrochemical Water Splitting. *Adv. Funct. Mater.* 2020;30:2003261. doi: 10.1002/adfm.202003261.
- [2] Zhu J, Hu L, Zhao P, Lee LYS, Wong KY. Recent Advances in Electrocatalytic Hydrogen Evolution Using Nanoparticles. *Chem. Rev.* 2020;120:851-918. doi: 10.1021/acs.chemrev.9b00248.
- [3] Zou X, Zhang Y. Noble metal-free hydrogen evolution catalysts for water splitting. *Chem. Soc. Rev.* 2015;44:5148-80. doi: 10.1039/c4cs00448e.
- [4] Anantharaj S, Ede SR, Sakthikumar K, Karthick K, Mishra S, Kundu S. Recent Trends and Perspectives in Electrochemical Water Splitting with an Emphasis on Sulfide, Selenide, and Phosphide Catalysts of Fe, Co, and Ni: A Review. *ACS Catal.* 2016;6:8069-97. doi: 10.1021/acscatal.6b02479.
- [5] Inocêncio CVM, Holade Y, Morais C, Kokoh KB, Napporn TW. Electrochemical Hydrogen Generation Technology: Challenges in electrodes materials for a Sustainable Energy. *Electrochem. Sci. Adv.* 2022: e2100206, In Press. doi: 10.1002/elsa.202100206
- [6] Hu C, Zhang L, Gong J. Recent progress made in the mechanism comprehension and design of electrocatalysts for alkaline water splitting. *Energy Environ. Sci.* 2019;12:2620-45. doi: 10.1039/c9ee01202h.
- [7] Anantharaj S, Noda S, Jothi V, Yi S, Driess M, Menezes P. Strategies and Perspectives to Catch the Missing Pieces in Energy-Efficient Hydrogen Evolution Reaction in Alkaline Media. *Angew Chem - Int. Ed.* 2021;60:18981-9006. doi: 10.1002/anie.202015738.
- [8] Mahmood N, Yao Y, Zhang JW, Pan L, Zhang X, Zou JJ. Electrocatalysts for Hydrogen Evolution in Alkaline Electrolytes: Mechanisms, Challenges, and Prospective Solutions. *Adv. Sci.* 2018;5. doi: 10.1002/advs.201700464.
- [9] Inocêncio CVM, Fouda-Onana F, Rousseau J, Guignard N, Napporn T, Morais C, Kokoh KB. A Step Forward: Hydrogen Production on Cobalt Molybdenum Sulfide Electrocatalyst in Anion Exchange Membrane Water Electrolyzer. *ACS Appl. Energy Mater.* 2022. in press. doi: 10.1021/acsaem.2c02270.
- [10] Anjum MAR, Jeong HY, Lee MH, Shin HS, Lee JS. Efficient Hydrogen Evolution Reaction Catalysis in Alkaline Media by All-in-One MoS₂ with Multifunctional Active Sites. *Adv. Mater.* 2018;30:1-9. doi: 10.1002/adma.201707105.
- [11] Jaramillo TF, Jørgensen KP, Bonde J, Nielsen JH, Horch S, Chorkendorff I. Identification of Active Edge Sites for Electrochemical H₂ Evolution from MoS₂ Nanocatalysts. *Science.* 2007;317:100-2. doi: 10.1126/science.1141483.
- [12] Hinnemann B, Moses PG, Bonde J, Jørgensen KP, Nielsen JH, Horch S, Chorkendorff I, Nørskov JK. Biomimetic hydrogen evolution: MoS₂ nanoparticles as catalyst for hydrogen evolution. *J. Amer. Chem. Soc.* 2005;127:5308-9. doi: 10.1021/ja0504690.

- [13] Fuel Cells and Hydrogen: From Fundamentals to Applied Research, Hacker V, Mitsushima S. Eds. Elsevier. 2018. doi: 10.1016/C2016-0-01053-7.
- [14] Huang G, Mandal M, Hassan NU, Groenhout K, Dobbs A, Mustain WE, Kohl PA. Ionomer Optimization for Water Uptake and Swelling in Anion Exchange Membrane Electrolyzer: Oxygen Evolution Electrode. *J. Electrochem. Soc.* 2020;167:164514. doi: 10.1149/1945-7111/abcde3.
- [15] Motealleh B, Liu Z, Masel RI, Sculley JP, Richard Ni Z, Meroueh L. Next-generation anion exchange membrane water electrolyzers operating for commercially relevant lifetimes. *Int. J. Hydrog. Energy.* 2021;46:3379-86. doi: 10.1016/j.ijhydene.2020.10.244.
- [16] Liu Z, Sajjad SD, Gao Y, Yang H, Kaczur JJ, Masel RI. The effect of membrane on an alkaline water electrolyzer. *Int. J. Hydrog. Energy.* 2017;42:29661-5. doi: 10.1016/j.ijhydene.2017.10.050.
- [17] Henkensmeier D, Najibah M, Harms C, Žitka J, Hnát J, Bouzek K. Overview: State-of-the Art Commercial Membranes for Anion Exchange Membrane Water Electrolysis. *J. Electrochem. Energy Convers. Storage.* 2021;18. doi: 10.1115/1.4047963.
- [18] Wang M, Zhang L, He Y, Zhu H. Recent advances in transition-metal-sulfide-based bifunctional electrocatalysts for overall water splitting. *J. Mater. Chem. A.* 2021;9:5320-63. doi: 10.1039/d0ta12152e.
- [19] Kabir S, Lemire K, Artyushkova K, Roy A, Odgaard M, Schlueter D, Oshchepkov A, Bonnefont A, Savinova E, Sabarirajan DC, Mandal P, Crumlin EJ, Zenyuk IV, Atanassov P, Serov A. Platinum group metal-free NiMo hydrogen oxidation catalysts: high performance and durability in alkaline exchange membrane fuel cells. *J. Mater. Chem. A.* 2017;5:24433-43. doi: 10.1039/c7ta08718g.
- [20] Faid AY, Xie L, Barnett AO, Seland F, Kirk D, Sunde S. Effect of anion exchange ionomer content on electrode performance in AEM water electrolysis. *Int. J. Hydrog. Energy.* 2020;45:28272-84. doi: 10.1016/j.ijhydene.2020.07.202.
- [21] Garsany Y, Baturina OA, Swider-Lyons KE, Kocha SS. Experimental Methods for Quantifying the Activity of Platinum Electrocatalysts for the Oxygen Reduction Reaction. *Anal. Chem.* 2010;82:6321-8. doi: 10.1021/ac100306c.
- [22] Benchakar M, Natu V, Elmelegy TA, Sokol M, Snyder J, Comminges C, Morais C, Célérier S, Habrioux A, Barsoum MW. On a Two-Dimensional MoS₂/Mo₂CT_x Hydrogen Evolution Catalyst Obtained by the Topotactic Sulfurization of Mo₂CT_x MXene. *J. Electrochem. Soc.* 2020;167:124507. doi: 10.1149/1945-7111/abad6e.
- [23] Mukherji A, Bal R, Srivastava R. Understanding the Co : Mo Compositional Modulation and Fe-Interplay in Multicomponent Sulfide Electrocatalysts for Oxygen and Hydrogen Evolution Reactions. *ChemElectroChem.* 2020;7:2740-51. doi: 10.1002/celec.202000314.
- [24] Ghoshal S, Pivovarov BS, Alia SM. Evaluating the effect of membrane-ionomer combinations and supporting electrolytes on the performance of cobalt nanoparticle anodes in anion exchange membrane electrolyzers. *J. Power Sources.* 2021;488:229433. doi: 10.1016/j.jpowsour.2020.229433.
- [25] Li Z, Xiao M, Zhou Y, Zhang D, Wang H, Liu X, Wang D, Wang W. Pyrite FeS₂/C nanoparticles as an efficient bi-functional catalyst for overall water splitting. *Dalton Trans.* 2018;47:14917-23. doi: 10.1039/c8dt02927j.

- [26] Joensen P, Crozier ED, Alberding N, Frindt RF. A study of single-layer and restacked MoS₂ by x-ray diffraction and x-ray absorption spectroscopy. *J. Phys. C: Solid State Phys.* 1987;20:4043-53. doi: 10.1088/0022-3719/20/26/009.
- [27] Niefind F, Bensch W, Deng M, Kienle L, Cruz-Reyes J, Del Valle Granados JM. Co-promoted MoS₂ for hydrodesulfurization: New preparation method of MoS₂ at room temperature and observation of massive differences of the selectivity depending on the activation atmosphere. *Appl. Catal. A: Gen.* 2015;497:72-84. doi: 10.1016/j.apcata.2015.03.003.
- [28] Xie J, Zhang H, Li S, Wang R, Sun X, Zhou M, Lou XW, Xie Y. Defect-Rich MoS₂ Ultrathin Nanosheets with Additional Active Edge Sites for Enhanced Electrocatalytic Hydrogen Evolution. *Adv. Mater.* 2013;25:5807-13. doi: 10.1002/adma.201302685
- [29] Inocência CVM, Rousseau J, Guignard N, Canaff C, Morisset S, Comminges C, Morais C, Kokoh KB. Taking Advantage of Teamwork: Unsupported Cobalt Molybdenum Sulfide as an Active HER Electrocatalyst in Alkaline Media. *J. Electrochem. Soc.* 2022;169:054524. doi: 10.1149/1945-7111/ac6b59.
- [30] Ulbrich KF, Souza BS, Campos CEM. Synthesis of n-hydrated nickel sulfates from mechanically alloyed nanocrystalline nickel sulfides. *Green Chem.* 2021;23:4580-93. doi: 10.1039/D1GC01213D
- [31] Wu Z, Huang L, Liu H, Li M, Wang H. Surface oxidation of transition metal sulfide and phosphide nanomaterials. *Nano Res.* 2020;14:2264-7. doi: 10.1007/s12274-020-3219-5
- [32] Wan K, Luo J, Zhou C, Zhang T, Arbiol J, Lu X, Mao B-W, Zhang X, Fransaer J. Hierarchical Porous Ni₃S₄ with Enriched High-Valence Ni Sites as a Robust Electrocatalyst for Efficient Oxygen Evolution Reaction. *Adv. Funct. Mater.* 2019;29:1-8. doi: 10.1002/adfm.201900315.
- [33] Yang SL, Yao HB, Gao MR, Yu SH. Monodisperse cubic pyrite NiS₂ dodecahedrons and microspheres synthesized by a solvothermal process in a mixed solvent: Thermal stability and magnetic properties. *CrystEngComm.* 2009;11:1383-90. doi: 10.1039/b900444k
- [34] Suzuki T, Uchinokura K, Sekine T, Matsuura E. Raman scattering of NiS₂. *Solid State Commun.* 1977;23:847-52. doi: 10.1016/0038-1098(77)90967-X.
- [35] Pham DV, Patil RA, Lin JH, Lai CC, Liou Y, Ma YR. Doping-free bandgap tuning in one-dimensional Magneli-phase nanorods of Mo₄O₁₁. *Nanoscale.* 2016;8:5559-66. doi: 10.1039/c5nr08118a
- [36] Dieterle M, Mestl G. Raman spectroscopy of molybdenum oxides. *Phys. Chem. Chem. Phys.* 2002;4:822-6. doi: 10.1039/b107046k.
- [37] Zoller M, Bubnova R, Biryukov Y, Haussühl E, Pöttgen R, Janka O, Penner S, Praty C, Fitzek H, Winkler J, Filatov S, Huppertz H. Elucidating the physical properties of the molybdenum oxide Mo₄O₁₁ and its tantalum substituted variant Mo₂Ta₂O₁₁. *Zeitschrift für Kristallographie - Cryst. Mater.* 2020;235:143-55. doi: 10.1515/zkri-2019-0073.
- [38] Kong D, Wang H, Cha JJ, Pasta M, Koski KJ, Yao J, Cui Y. Synthesis of MoS₂ and MoSe₂ films with vertically aligned layers. *Nano Lett.* 2013;13:1341-7. doi: 10.1021/nl400258t.
- [39] Lee JU, Park J, Son YW, Cheong H. Anomalous excitonic resonance Raman effects in few-layered MoS₂. *Nanoscale.* 2015;7:3229-36. doi: 10.1039/c4nr05785f.

- [40] Politano GG, Castriota M, Santo MPD, Pipita MM, Desiderio G, Vena C, Versace C. Physical Investigation of Spin-Coated MoS₂ Films. *Mater. Proc.* 2020;4:3. doi: 10.3390/iocn2020-08005.
- [41] Mignuzzi S, Pollard AJ, Bonini N, Brennan B, Gilmore IS, Pimenta MA, Richards D, Roy D. Effect of disorder on Raman scattering of single-layer MoS₂. *Phys. Rev. B.* 2015;91. doi: 10.1103/PhysRevB.91.195411.
- [42] Xu X, Liang L, Zhang X, Xing X, Zhao Y, Gao J, Wei A. Design of reduced graphene oxide supported NiMoS₄ to enhance energy capacity of hybrid supercapacitors. *Colloids and Surfaces A: Physicochemical and Engineering Aspects.* 2020;586:124289. doi: 10.1016/j.colsurfa.2019.124289
- [43] Sathiyaraj E, Gurumoorthy G, Thirumaran S. Nickel(ii) dithiocarbamate complexes containing the pyrrole moiety for sensing anions and synthesis of nickel sulfide and nickel oxide nanoparticles. *New J. Chem.* 2015;39:5336-49. doi: 10.1039/C4NJ02250E
- [44] Bocquet AE, Mamiya K, Mizokawa T, Fujimori A, Miyadai T, Takahashi H, Mōri M, Suga S. Electronic structure of 3d transition metal pyrites MS₂ (M = Fe, Co or Ni) by analysis of the M 2p core-level photoemission spectra. *J. Phys.: Condens. Matter.* 1996;8:2389-400. doi: 10.1088/0953-8984/8/14/013.
- [45] Guichard B, Roy-Auberger M, Devers E, Legens C, Raybaud P. Aging of Co(Ni)MoP/Al₂O₃ catalysts in working state. *Catal. Today.* 2008;130:97-108. doi: 10.1016/j.cattod.2007.09.007.
- [46] Rickman JT, Linton RW. Surface and depth profiling techniques using XPS applied to the study of nickel-containing environmental particles. *Appl. Surface Sci.* 1993;68:375-93. doi: 10.1016/0169-4332(93)90260-I.
- [47] Muijsers JC, Weber T, van Hardeveld RM, Zandbergen HW, Niemantsverdriet JWH. Sulfidation study of molybdenum oxide using MoO₃/SiO₂/Si(100) model catalysts and Mo₃(IV)-sulfur cluster compounds. *J. Catal.* 1995;157:698-705. doi: 10.1006/jcat.1995.1335.
- [48] Zhang J, Wang T, Liu P, Liu S, Dong R, Zhuang X, Chen M, Feng X. Engineering water dissociation sites in MoS₂ nanosheets for accelerated electrocatalytic hydrogen production. *Energy Environ. Sci.* 2016;9:2789-93. doi: 10.1039/c6ee01786j.
- [49] Zhang B, Liu J, Wang J, Ruan Y, Ji X, Xu K, Chen C, Wan H, Miao L, Jiang J. Interface engineering: The Ni(OH)₂/MoS₂ heterostructure for highly efficient alkaline hydrogen evolution. *Nano Energy.* 2017;37:74-80. doi: 10.1016/j.nanoen.2017.05.011.
- [50] Oener SZ, Foster MJ, Boettcher SW. Accelerating water dissociation in bipolar membranes and for electrocatalysis. *Science.* 2020;369:1099-103. doi: 10.1126/science.aaz1487.
- [51] Xu D, Stevens MB, Cosby MR, Oener SZ, Smith AM, Enman LJ, Ayers KE, Capuano CB, Renner JN, Danilovic N, Li Y, Wang H, Zhang Q, Boettcher SW. Earth-Abundant Oxygen Electrocatalysts for Alkaline Anion-Exchange-Membrane Water Electrolysis: Effects of Catalyst Conductivity and Comparison with Performance in Three-Electrode Cells. *ACS Catal.* 2019;9:7-15. doi: 10.1021/acscatal.8b04001.
- [52] Voiry D, Salehi M, Silva R, Fujita T, Chen M, Asefa T, Shenoy VB, Eda G, Chhowalla M. Conducting MoS₂ Nanosheets as Catalysts for Hydrogen Evolution Reaction. *Nano Lett.* 2013;13:6222-7. doi: 10.1021/nl403661s.

- [53] Lukowski MA, Daniel AS, Meng F, Forticaux A, Li L, Jin S. Enhanced hydrogen evolution catalysis from chemically exfoliated metallic MoS₂ nanosheets. *J. Amer. Chem. Soc.* 2013;135:10274-7. doi: 10.1021/ja404523s.
- [54] Huang S, Ma D, Hu Z, He Q, Zai J, Chen D, Qiao Q, Wu M, Qian X. Synergistically Enhanced Electrochemical Performance of Ni₃S₄-PtX (X = Fe, Ni) Heteronanorods as Heterogeneous Catalysts in Dye-Sensitized Solar Cells. *ACS Appl Mater Interfaces.* 2017;9:27607-17. doi: 10.1021/acsami.7b05418.
- [55] Benck JD, Hellstern TR, Kibsgaard J, Chakthranont P, Jaramillo TF. Catalyzing the hydrogen evolution reaction (HER) with molybdenum sulfide nanomaterials. *ACS Catal.* 2014;4:3957-71. doi: 10.1021/cs500923c.
- [56] Rudi S, Cui C, Gan L, Strasser P. Comparative Study of the Electrocatalytically Active Surface Areas (ECSAs) of Pt Alloy Nanoparticles Evaluated by Hupd and CO-stripping voltammetry. *Electrocatalysis.* 2014;5:408-18. doi: 10.1007/s12678-014-0205-2.
- [57] Li D, Chung HT, Maurya S, Matanovic I, Kim YS. Impact of ionomer adsorption on alkaline hydrogen oxidation activity and fuel cell performance. *Curr. Opin. Electrochem.* 2018;12:189-95. doi: 10.1016/j.coelec.2018.11.012.
- [58] Bates MK, Jia Q, Ramaswamy N, Allen RJ, Mukerjee S. Composite Ni/NiO-Cr₂O₃ Catalyst for Alkaline Hydrogen Evolution Reaction. *J. Phys Chem C.* 2015;119:5467-77. doi: 10.1021/jp512311c.